

CZECH TECHNICAL UNIVERSITY IN PRAGUE

Multidimensional Hydrodynamic Plasma Simulations and X-Ray Radiation Generation

by

Martin Šach

A research report at

Faculty of Nuclear Sciences and Physical Engineering

Department of Physics

Supervisor: **doc. Ing. Milan Kuchařík, Ph.D.**

Consultants: **Ing. Jan Nikl, Ing. Miroslav Krůs, Ph.D.**

Field of study: **Physics and Technology of Thermonuclear Fusion**

September 2020

Prohlášení

Prohlašuji, že jsem svou bakalářskou práci vypracoval samostatně a použil jsem pouze podklady (literaturu, projekty, SW atd...) uvedené v příloženém seznamu.

Nemám závažný důvod proti použití tohoto školního díla ve smyslu § 60 Zákona č. 121/2000 Sb., o právu autorském, o právech souvisejících s právem autorským a o změně některých zákonů (autorský zákon).

V Praze dne 16. 9. 2020

.....

podpis

CZECH TECHNICAL UNIVERSITY IN PRAGUE

Abstract

Multidimensional Hydrodynamic Plasma Simulations and X-Ray Radiation Generation

Author: Martin Šach

Supervisor: doc. Ing. Milan Kuchařík, Ph.D. Department of Physical Electronics,
Czech Technical University in Prague

Consultant: Ing. Jan Nikl ELI Beamlines, Institute of Physics of CAS, Ing. Miroslav
Krůs, Ph.D. Institute of Plasma Physics of CAS

In this report, the processes involved in X-ray amplification in plasma-based gain medium are studied. The plasma is assumed to be generated via interaction of a laser beam with a solid iron target. Both the interaction of laser with solid target and the x-ray amplification are being simulated. Particular focus is put on the radiation propagation and energy exchange. A ray tracing procedure is implemented to simulate the phenomena. The resonant absorption, bremsstrahlung and x-ray gain models are taken into account. The X-ray gain model is based on M -level system of rate equations in neon like iron. The algorithm is developed for a general mesh, to enable integration to both, finite difference and finite element, hydrodynamic codes operating on Lagrangian grids. The results of the M -level model of gain are evaluated and several ray tracing simulations are performed to demonstrate the capabilities of the developed method.

Acknowledgements

I would like to express my gratitude to my supervisor doc. Milan Kuchařík for providing his patient guidance as well as constant encouragement. I would also like to give special thanks to my consultant Ing. Jan Nikl for his insightful advice, without him this study would not be possible.

Contents

1	Introduction	1
2	Direction of radiation propagating in plasmas	3
2.1	Geometric optics approximation	3
2.2	Snell's law in vector form	4
2.3	Refractive index of cold plasmas	4
3	Absorption of radiation propagating in plasma	6
3.1	Energy distribution in many ray approximation	7
3.2	Laser absorption model	7
3.2.1	Inverse bremsstrahlung	7
3.2.2	Resonance absorption	8
3.3	X-ray amplification model	9
3.3.1	Verification of numerical results	12
3.3.2	Comparison with previous results	12
4	Domain discretization	15
4.1	Basic concepts	15
4.2	Discretization schemes	15
5	Electron density gradient estimation	17
5.1	Local reconstruction using a least squares method	17
6	Ray tracing algorithm for general meshes	19
6.1	Ray trajectories computation	19
6.2	Comparison with the direct integration	21
6.3	Ray energy exchange estimation	24
7	Simulations of radiation propagation	26
7.1	Results of 1D hydrodynamic simulation	26
7.2	Gain prediction in 1D hydrodynamic simulation	27
7.3	Extension of the 1D results to 2D	29
7.4	Driving laser absorption simulation	30
7.5	X-ray gain simulations in laser generated plasma	32
8	Conclusion	35
	Bibliography	36

Chapter 1

Introduction

A source of intensive coherent x-ray radiation has the potential to play a crucial role in various fields ranging from biology to fundamental physics [19]. Among notable application, are high resolution holographic microscopy, microlithography for production of micro scale computer chips and tomographic imaging of molecular orbitals to name a few [22].

Multiple different approaches to x-ray radiation generation are currently available, where one of the most successful methods is the so called Free Electron Laser (FEL) [19]. A device that uses relativistic electron as a gain medium. This work concerns a different approach, a plasma amplification medium based soft X-ray laser. The idea is to use a plasma generated by a conventional laser pulse as a gain medium for a X-ray pulse to amplify it. The weak X-ray pulse created by other means (usually by higher harmonics generation) is called a seed. In general the driving laser is incident on a solid target under an angle. Here it is assumed that the driving laser is placed perpendicular to the target and that the seeding pulse traverses the created plasma in direction parallel to the target surface. The geometry of this approach is summarized in Fig 1.1.

This work is a continuation of our previous effort to simulate the process [22]. In the previous work, the plasma conditions, generated by laser interacting with a solid iron target, were simulated using a hydrodynamic approach in one dimension. This work is aimed at implementing a sufficient model of laser plasma interaction and radiation propagation. A ray tracing approach described in [21] is taken. It is intended, that the implemented algorithm is used for both driving laser absorption estimation and X-ray seed amplification evaluation in multi dimensional hydrodynamic simulations [12], [16].

To accurately model the x-ray amplification, a new model of x-ray gain using the coefficients obtained using the Flexible Atomic Code (FAC) [9] is implemented. This

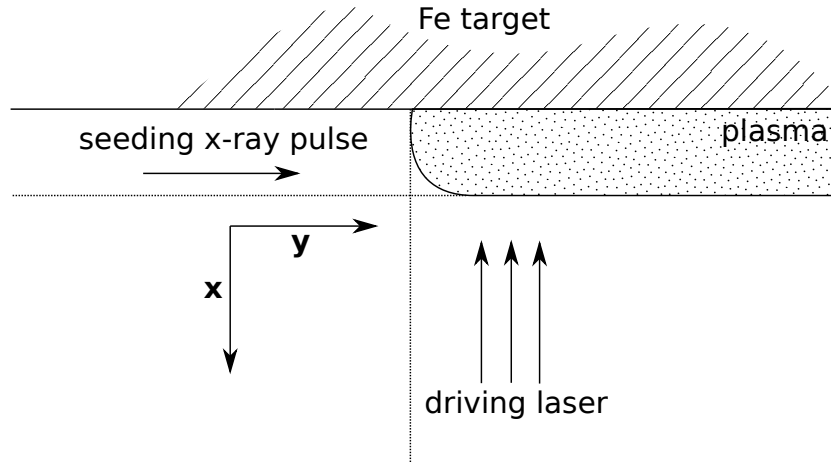


FIGURE 1.1: The geometry of plasma generated by the driving laser as an amplification medium for the seeding X-ray pulse

model takes into account M electron energy levels as opposed to the previous approach inspired by [19], where only 3 energy levels were used, leading to a significantly more realistic estimates.

In [chapter 2](#) a theoretical framework of the work is established. A geometric optics approximation is introduced and a model of cold plasma is used to describe the plasma properties relevant to radiation propagation. This is further expanded in [chapter 3](#), where a general approach to plasma and radiation interaction is described. Most notably in this chapter a M -level x-ray amplification model is introduced and its predictions are compared to the previous model [22].

The basic domain discretization techniques used in hydrodynamic simulations relevant to this work are presented in [chapter 4](#) and following up on this a gradient estimation method is summarized in [chapter 5](#).

All the previous partial results are gathered in [chapter 6](#) to form a ray tracing algorithm for general meshes with energy exchange estimation as post processing of the trajectories. This algorithm is used in [chapter 7](#) to perform simple simulations in 1D results extended to 2D by assuming a symmetry. The goal of these simulations is to demonstrate the capability of the implemented methods to be used for both driving laser absorption and X-ray laser amplification.

Chapter 2

Direction of radiation propagating in plasmas

In this chapter a basic model of laser propagation is reviewed. Throughout the text, the laser is described as a set of independent laser rays, each carrying a part of the original laser beam energy. This enables separate treatment of each ray via the framework of geometric optics approximation. Numerical methods employing such approximation is usually referred to as ray tracing. It relies on the knowledge of index of refraction, described at the end of this chapter.

2.1 Geometric optics approximation

In the geometric optics approximation, the wave properties of radiation are neglected. It is thus necessary that the plasma characteristic scales are large compared to the wavelength λ of the propagating radiation [2].

Ray equation governing the ray trajectory in given media states that [2]

$$\frac{d}{ds} \left(n \frac{d\vec{r}}{ds} \right) = \nabla n. \quad (2.1)$$

Here s is a parameter measured along the trajectory of the ray, \vec{r} are the coordinates the of trajectory points and n is the index of refraction evaluated at the trajectory points.

2.2 Snell's law in vector form

A special case of ray propagation encountered in ray tracing simulations is a ray passing through an interface of two isotropic media. The refraction will occur in a plane and it can be derived from the ray equation (2.1), that the relation between the angle of incidence θ_1 and angle of refraction θ_2 measured from the normal to the boundary is given by [2]

$$\sin \theta_1 n_1 = \sin \theta_2 n_2, \quad (2.2)$$

where n_1 and n_2 are the indices of refraction. This is what is usually referred to as the Snell's law. Combined with the law of reflection, it provides a full description of the situation in terms of ray direction.

Although this form is very simple and can be directly used to perform energy deposition simulations [21], but assumptions that the refraction occurs in a plane and that the angles are measured from the interface normal, must be taken into account during the algorithm implementation. To simplify the implementation to actual simulations, especially in three dimensions, a vector form of Snell's law is used [8]. Denoting

$$c = \cos \theta_1 = -\vec{n} \cdot \vec{l}, \quad (2.3)$$

where l is a unit vector in a direction of the incidence ray and n is the unit normal to the interface. As there are two options for the unit normal, the one for which $c \geq 0$ is taken. Further designating $r = n_1/n_2$, it can be shown that vector form of Snell's law is

$$\vec{d} = r\vec{l} + \left(rc - \sqrt{1 - r^2(1 - c^2)} \right) \vec{n}, \quad (2.4)$$

where \vec{d} is the direction of the refracted ray. This formulation also provides an insight to total reflection as for $1 - r^2(1 - c^2) < 0$ there is no refracted ray. This can only happen for $n_1 > n_2$.

2.3 Refractive index of cold plasmas

A model taken over from [21] for index of refraction is used. It holds for collisional cold plasma approximation and states that plasma permittivity is

$$\varepsilon = 1 - \frac{\omega_p^2}{\omega^2 + \nu_{ei}^2} + i \frac{\nu_{ei}}{\omega} \frac{\omega_p^2}{\omega^2 + \nu_{ei}^2}, \quad (2.5)$$

where ν_{ei} is the collisional frequency, ω is the angular frequency of the laser, ω_p is the electron plasma frequency

$$\omega_p^2 = \frac{4\pi e^2 n_e}{m_e}. \quad (2.6)$$

Spitzer formula [6] extended for low energies is used to determine the collisional frequency

$$\nu_{ei} = \frac{4}{3} \frac{\sqrt{2\pi} Z e^4 n_e \ln \Lambda}{\sqrt{m_e} (k_b T_e + E_f)^{3/2}}, \quad (2.7)$$

where Z is the average ionization, e is the electron charge, n_e is the electron density, m_e is the mass of electron, k_b is the Boltzmann constant, T_e is electron temperature. Furthermore $\ln(\Lambda)$ is the Coulomb logarithm

$$\ln(\Lambda) = \max \left(2, \ln \sqrt{\frac{b_{max}}{b_{min}}} \right), \quad (2.8)$$

where

$$b_{max} = \frac{\sqrt{\frac{k_b T_e}{m_e}}}{\max(\omega, \omega_p)} \quad b_{min} = \max \left(\frac{Z e^2}{k_b T_e}, \frac{\hbar}{\sqrt{k_b T_e / m_e}} \right). \quad (2.9)$$

Finally, E_F is the Fermi energy [21]

$$E_F = \frac{\hbar^2}{2m_e} (3\pi^2 n_e)^{2/3}, \quad (2.10)$$

where \hbar is the reduced Planck constant.

To obtain the index of refraction, it is assumed that the relative permeability μ of examined plasma is close to a unity, thus it follows that

$$n = \text{Re}(\sqrt{\varepsilon\mu}) = \text{Re}(\sqrt{\varepsilon}). \quad (2.11)$$

Note that ε is a complex number in general. The index of refraction corresponds to the real part $\text{Re}(\sqrt{\varepsilon})$. The significance of the $\text{Im}(\sqrt{\varepsilon})$ is clarified in [chapter 3](#).

Chapter 3

Absorption of radiation propagating in plasma

In the previous chapter, trajectories of rays obtained by the decomposition of the laser beam were discussed. To complete the model of radiation propagation, an approximation of energy exchange between plasmas and radiation is necessary. In case of a driving laser interacting with a solid target, absorption is the most important aspect. On the other hand, to model refraction effects in gain estimating simulations, radiation amplification is the main subject of interest. Both are described in this chapter. Common ground for all the models is the transfer equation [11]

$$\frac{dI(t, \vec{r})}{ds} = j(t, \vec{r}) - k(t, \vec{r})I(t, \vec{r}), \quad (3.1)$$

where I is the intensity of laser ray at given time and space, j is the emissivity coefficient of the media, k is the absorption coefficient and s is the parameter along the trajectory of the ray. Assuming a homogeneous media and thus j and k constant, this equation can be integrated over area ΔS_i and time Δt similarly to (3.5). Further neglecting the emissivity j of the media, an equation for energy of the radiation is obtained [21]

$$\frac{dE_{\Delta t \Delta S_i}}{ds} = -kE_{\Delta t \Delta S_i}. \quad (3.2)$$

In homogeneous media, its solution can be easily written in terms of energy absorbed in the media ΔE and length of path the ray traced in this media l

$$\Delta E = E_{in} (1 - \exp(-kl)), \quad (3.3)$$

where E_{in} is the energy of the ray entering the medium.

3.1 Energy distribution in many ray approximation

A laser beam is usually described by its intensity $I(t, \vec{r})$, which in general case varies in time and space. Now given an arbitrary small time interval Δt , the laser at the beginning, before absorption, carries a fraction of total energy $E_{0\Delta t}$ given by the spatial and temporal distribution of intensity,

$$E_{0\Delta t} = \int_t^{t+\Delta t} \int_S I(\tau, \vec{r}) d\vec{r} d\tau \quad (3.4)$$

where S is a closed surface encapsulating the source. In the case of laser, a surface close to the origin can be chosen. This surface is the idealized spatial cross section of the laser beam. To discretize the laser into N rays, the cross section is divided into N areas ΔS_j , where index j denotes a single ray. Each ray is associated energy equal to

$$E_{0\Delta t \Delta S_j} = \int_t^{t+\Delta t} \int_{\Delta S_j} I(\tau, \vec{r}) d\vec{r} d\tau. \quad (3.5)$$

It follows that the sum of energies of each ray is the total initial energy of the laser beam at a given time step

$$E_{0\Delta t} = \sum_{j=1}^N E_{0\Delta t \Delta S_j}. \quad (3.6)$$

In practice usually a homogeneous division of S is taken.

3.2 Laser absorption model

Laser radiation absorption model used in this work is adopted from [21]. Here only the main points are summarized. Detailed treatment is presented in the mentioned work. Two major mechanisms taken into account are bremsstrahlung and resonant absorption.

3.2.1 Inverse bremsstrahlung

Radiation emitted by collisions of charged particles is called bremsstrahlung, from term for breaking radiation. An inverse process to this, during which an electron absorbs a photon while colliding with another charged particle, is called inverse bremsstrahlung [7].

Following the conclusions of [21], the inverse bremsstrahlung absorption coefficient k is set to be

$$k_{ib} = \frac{2\omega}{c} \text{Im}\sqrt{\varepsilon}, \quad (3.7)$$

where ω is the angular frequency of the laser, c is the speed of light and ε is the permittivity specified by equation (2.5).

3.2.2 Resonance absorption

If there exists a non-zero electric field component of the electromagnetic wave in the direction of plasma electron density gradient, an evanescent plasma wave around the area of critical density is resonantly excited and energy is absorbed. This is known as resonant absorption and depends on the polarization of the incident radiation. In case of the electric field vector polarized in the plane of incidence, usually referred to as p-polarization, the effect is maximal and a part of the laser energy is resonantly absorbed at the laser turning point. On the other hand if the electric field vector is polarized perpendicular to the plane of incidence, usually referred to as s-polarization, no resonant absorption occurs [20].

For p-polarization, an approximate analytical model devised by [20] is used. It states that

$$\Delta E = aE_{in}, \quad (3.8)$$

$$a = 18q \frac{\text{Ai}^3(q)}{|\text{Ai}'(q)|}, \quad (3.9)$$

$$q = \left(\frac{2\pi}{\lambda} L_{char} \right)^{2/3} \sin^2 \varphi_{in}, \quad (3.10)$$

$$L_{char} = \frac{n_e^{crit}}{|\text{grad } n_e|^{crit}}, \quad (3.11)$$

where

$$n_e^{crit} = \frac{m_e \pi c^2}{e^2 \lambda^2}. \quad (3.12)$$

Here n_e is called the critical density, m_e is the mass of electron, c is the speed of light, e is elemental charge, $\lambda = 2\pi c/\omega$ is the wavelength of incident radiation and Ai is the Airy function. Further note, that $|\text{grad } n_e|^{crit}$ is the magnitude of electron density gradient evaluated at the point of critical density. Finally φ_{in} is the angle between the incident ray and the gradient of electron density. For sake of implementation, $\sin^2 \varphi_{in}$ can be expressed in terms of the directional vectors of the ray and the gradient

$$\sin^2 \varphi_{in} = 1 - \cos^2 \varphi_{in} = 1 - \left(\vec{l} \cdot \vec{g} \right)^2, \quad (3.13)$$

where \vec{l} is the direction of the ray and \vec{g} is the direction of the electron density gradient. Both of these vectors magnitudes are normalized.

Now, to avoid numerical calculations of the Airy functions, an approximate relation introduced in [21] is used for a

$$a = q \frac{\exp(-\frac{4}{3}q^{3/2})}{q + 0.48} \frac{\pi}{2}. \quad (3.14)$$

Altogether, the model states that

$$\Delta E = q \frac{\exp(-\frac{4}{3}q^{3/2})}{q + 0.48} \frac{\pi}{2} E_{in} \quad (3.15)$$

is the amount of energy being absorbed at the radiation turning point, due to resonant excitation of plasma waves, given that the radiation is fully p-polarised.

3.3 X-ray amplification model

The absorption coefficient k in equation (3.1) may not be positive. The negative coefficient k is usually replaced by the so called gain coefficient g [11]. This leads to modification of equation (3.3)

$$\Delta E = E_{in}(1 - \exp(gl)). \quad (3.16)$$

As in this notation the ΔE is negative, a new quantity E_g is used, the radiation energy gain

$$\Delta E_g = E_{in}(\exp(gl) - 1). \quad (3.17)$$

In the previous work [22], the gain coefficient has been estimated for a specific x-ray transition in and electron shell of neon-like iron. The transition of interest has been

$$2p_{1/2}^5 3s_{1/2}, J = 1 \longrightarrow 2p_{1/2}^5 3p_{1/2}, J = 0 \quad (3.18)$$

based on the simulations described in [19]. Throughout the work, the jj -coupling notation is used the same way as it is used in [9].

To estimate the gain coefficient of x-ray radiation, an inversion in atomic level populations at the transition of interest is required. Assuming that the Einstein coefficient for stimulated emission B_{21} can be expressed in terms of weighted oscillator strength $g_1 f_{12}$, where g_1 is the degeneration of the lower level and supposing that the profile function is approximated by $\frac{1}{\Delta\nu}$, $\Delta\nu$ being the broadening of the spectral line, commonly used

simplification [11], the gain coefficient can be estimated as

$$g = \frac{\pi e^2}{cm_e} g_1 f_{12} \left(\frac{N_2}{g_2} - \frac{N_1}{g_1} \right) \frac{1}{\nu}. \quad (3.19)$$

Here, e is the elemental charge, c is the speed of light, m_e is mass of electron, N_2/g_2 is the population density of upper level, where g_2 is the degeneration of this level and N_1/g_1 is the population density of lower level, where g_1 is the degeneration of lower level.

To accurately estimate the gain coefficient, the weighted oscillator strength $g_1 f_{12}$, line broadening $\Delta\nu$ and level populations $\frac{N_1}{g_1}$, $\frac{N_2}{g_2}$ are needed.

Line broadening is obtained from the Doppler and Lorentz broadening models described in the previous work [22]. For the Doppler width the following formula is used

$$\Delta\nu_{FWHM}^D = \frac{1}{2\sqrt{\ln 2}} \nu \sqrt{\frac{2kT_i}{m_u c^2}}, \quad (3.20)$$

where ν is the frequency of transition of interest, k is the Boltzmann constant, T_i is the ion temperature, m_u is the atomic mass unit and c is the speed of light. To estimate the effect of Lorentz broadening the following relation is used

$$\Delta\nu_{FWHM}^L = \alpha n_e^2 T_e^{-1/2}, \quad (3.21)$$

where n_e is the electron density, T_e electron temperature and constant α is chosen in such a way that the predictions match those of [10]. Altogether the profile function has the form

$$\frac{1}{\Delta\nu} = \frac{1}{\Delta\nu_{FWHM}^D + \Delta\nu_{FWHM}^L}. \quad (3.22)$$

The weighted oscillator strength and level populations are estimated using the Flexible atomic code (FAC) [9]. Weighted oscillator strength is simply a function of given transition and can be directly obtained. Situation is more complicated when it comes to the level populations. As the inversion in level populations is required to simulate a media with positive gain coefficient, Boltzmann distribution of electron populations can not be used as the system is not in an equilibrium. Instead, a solution of a system of rate equations must be found [11]. This has been previously done using a simple three level system introduced in [10]. Here a full M-level system is solved in the quasi-static approximation [11].

Density of electrons at a given energy level changes due to various collisional and radiative processes. In this work, collisional excitation, collisional deexcitation governed

by Einstein coefficient C_{ij} respectively C_{ji} and radiative deexcitation governed by Einstein coefficient A_{ji} are assumed to be the main contributions to level population and depopulation. Indices i, j , where $j > i$, denote arbitrary levels between which a transition is not forbidden. Other processes such as ionizing collisions, photo-recombination, photoexcitation and photoabsorption and three-body recombination are neglected not included. This may be a source of error and should be properly addressed in future work.

The rate of population/depopulation of a level can be summarized by equation [11]

$$\frac{dN_i}{dt} = \sum_{j>i} N_j A_{ji} - N_i \sum_{l<i} A_{il} + \sum_k N_k C_{ki} - N_i \sum_m C_{im}, \quad (3.23)$$

where N_i is the population density of the particular level i . Coefficient A_{ij} is a probability specific for each transition and does not depend on state variables, coefficient C_{ij} is a probability of collisional excitation/deexcitation governed by collisional cross-section $\langle \sigma_{ij} v \rangle$

$$C_{ij} = n_e \langle \sigma_{ij} v \rangle, \quad (3.24)$$

where n_e is the electron density. In this work, electron distribution is considered as Maxwellian and thus the coefficient C_{ij} is a function of temperature and electron density.

Using the quasi-static approximation that assumes level populations to vary slowly with population times, it is possible to form a set of equations for a given small dt and M energy levels

$$\frac{dN_i}{dt} = 0, \quad i = 1, 2, \dots, M. \quad (3.25)$$

This system has no unique solution, as can be seen from equation (3.23). If \vec{a} is the solution of the system, then $C\vec{a}$ is also a solution, where C is a real constant. To obtain a unique solution a condition

$$N_1 + N_2 + \dots + N_M = f_a n_i \quad (3.26)$$

must be satisfied, where n_i is the total ion density and f_a the fractional abundance of ion of interest. Fractional abundance is a function of ion temperature and is also obtained using FAC.

Using the mentioned Flexible atomic code (FAC) [9], the values of the Einstein coefficients are found based on the numerical solutions of the Dirac equation and input state variables from a hydrodynamic simulation. The quasi-static system is formed and solved also using FAC.

3.3.1 Verification of numerical results

To ensure the model is properly implemented and to demonstrate its usage, a set of relative populations at the level $2p_{1/2}^5 3p_{1/2}, J = 0$ in neon-like germanium has been evaluated for a given set of state variables. Following the results in [1] it has been done for electron densities ranging from 10^{20} cm^{-3} to 10^{23} cm^{-3} and set of temperatures 650, 850, ..., 1850 eV. The results are presented in Fig. 3.1.

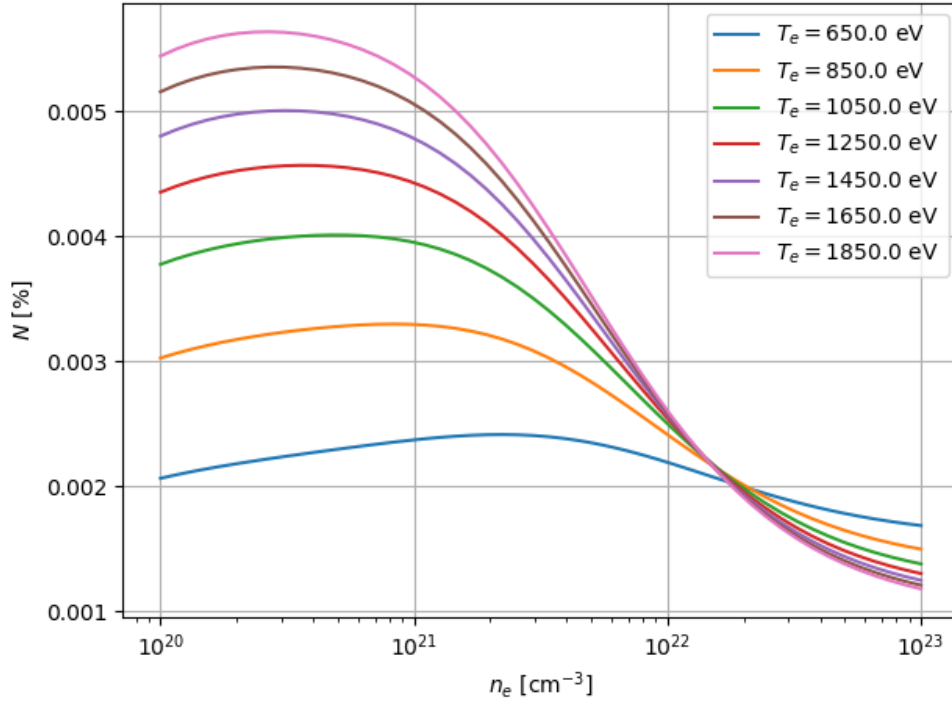


FIGURE 3.1: Relative populations N of $2p_{1/2}^5 3p_{1/2}, J = 0$ in neon-like germanium at various temperatures T_e as a function electron density n_e

Comparing the graphs of the results it is possible to conclude that the predicted relative populations are identical to results in [1]. This must be the case, as same methods have been used. This test thus serves as a sanity check of the method implementation.

3.3.2 Comparison with previous results

To compare the full M-level method with the previous results using the three-level system [22], the gain coefficient g is estimated for temperatures in the range of 150 - 850 eV and the densities in the range of $10^{19} - 10^{23} \text{ cm}^{-3}$. The same ion and electron temperatures are taken. This is done for transition (3.18) in neon like iron. The result is shown in Fig. 3.2.

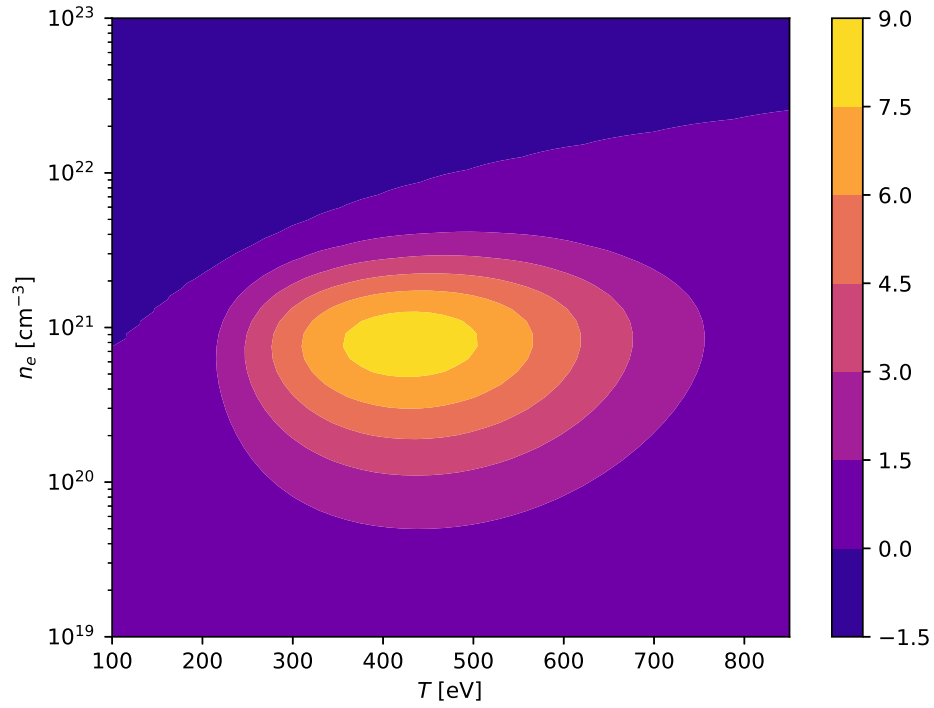


FIGURE 3.2: Gain coefficient as a function of temperature T and electron density n_e

Gain coefficient maximum is around 9 cm^{-1} and is achieved for density $7.5 \times 10^{20} \text{ cm}^{-3}$ and temperature 421 eV. In the previous work the maximum was predicted for density $3.6 \times 10^{20} \text{ cm}^{-3}$ and temperature 521 eV and it was around 48 cm^{-1} .

Compared to the previous work, the gain area is elongated along the density scale and logarithmic scale had to be used for electron density. This is expected as stated in [10] when comparing a three level model with the full M-level model. Otherwise the profile is remarkably similar, considering the simplicity of a three level system. The absolute values of gain differ by approximately a factor of five. It was expected that the gain coefficient predicted by M-level system will be lower although the factor of five is surprising and will be a subject of future study.

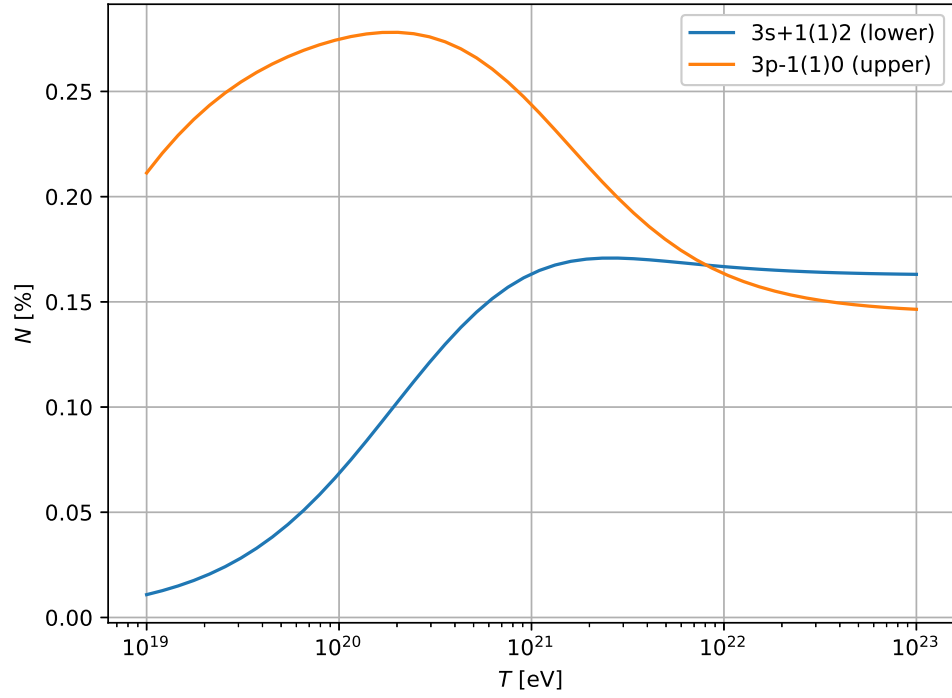


FIGURE 3.3: Population at the upper and lower energy levels as a function of density at temperature 421 eV

Using the M-level model, negative values of gain coefficient can be obtained. These are obtained if there is no longer a population inversion. This can be clearly seen in a graph of populations at the upper and lower energy levels as function of electron density. Temperature of 421 eV, at which the maximal gain is observed, is chosen and the graph is shown Fig. 3.3. The threshold where the inversion is 0 is at $8.1 \times 10^{21} \text{ cm}^{-3}$. This is consistent with the expectation that there exist a threshold electron density at which the inversion no longer occurs [10].

Chapter 4

Domain discretization

As the implemented algorithm is intended to be used in various hydrodynamic codes, it is necessary to introduce the different discretization practices. The emphasis is on the Lagrangian coordinates as these are used in targeted codes.

4.1 Basic concepts

In the Lagrangian coordinates the system is described using the Lagrangian coordinate X and time t . The coordinate X uniquely indicates a single fluid element and t is time. For detailed explanation of how to transform a system in the Eulerian coordinates to the Lagrangian coordinates, see [\[22\]](#).

For this work, a concept of face is also necessary. The definition of face varies with the number of dimensions. In 1D face is just a node between two cells, in 2D face is a line prescribed by two nodes between two cells and in 3D face is a surface prescribed by at least three nodes between two cells. For 2D visual representation of a Lagrangian mesh, see [Fig. 4.1](#).

4.2 Discretization schemes

In the finite difference method used in PALE a staggered scheme [\[3\]](#) is used. It states that, state values such as density, temperature, ionization etc. are in cell centers (cells being the fluid elements) and velocities are prescribed at nodes.

In finite element codes such as PETE2 [\[17\]](#)[\[15\]](#), the state values and flow rates are defined in different finite element spaces. It is the space of piece-wise constant functions

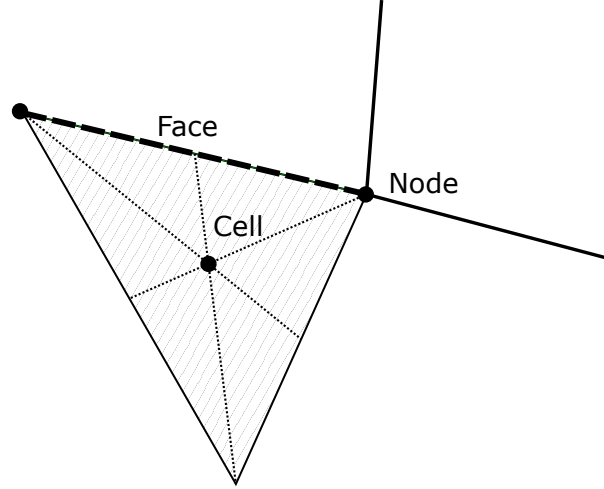


FIGURE 4.1: 2D visual aid for definition of cell centroid where state variables are located, nodes where flow rates are located and a notion of face

L_2 for state variables and space of piece-wise linear functions H_1 for kinetic variables [5]. In lowest order finite elements, this is equivalent to the staggered scheme used in finite difference methods.

As the ray tracing code aims algorithm aims to be as general as possible, various mesh types have to be taken into account. In 2D, the focus is mainly on triangle and quadrilateral discretization, although in theory the algorithm could be used for arbitrary polygons. It is intended to use the algorithm in PALE, where quadrilateral staggered discretization is used [13] and PETE2 where both triangular and quadrilateral finite elements can be used [16].

Chapter 5

Electron density gradient estimation

The knowledge of the electron density gradient direction at any point of a face is crucial for the ray tracing algorithm, as it is further explained in [chapter 6](#). To be able to evaluate the amount of energy absorbed due to resonant absorption using the equation (3.15), the magnitude of electron density gradient is needed.

5.1 Local reconstruction using a least squares method

The task is to reconstruct the gradient from electron density n_e defined in the centroids of cells. Local reconstruction algorithm proposed in [18] is used. The derivation is done in 2D. First the gradients at nodes are reconstructed. This is done by fitting a linear polynomial

$$n_e(x, y) = n_e^i + \overline{\partial_x n_e^i}(x - x_i) + \overline{\partial_y n_e^i}(y - y_i), \quad (5.1)$$

around a node i over a cells adjacent to i , where (x_i, y_i) is the location of the node. Consider l to be one of the adjacent cells, then the polynomial evaluated at the centroid of l is $n_e^l = n_e(x_l, y_l)$, where (x_l, y_l) is the cell centroid location. Note that there are actually three unknowns in the equation as the density at the node location is also unknown. The unknown vector is thus $(n_e^i, \overline{\partial_x n_e^i}, \overline{\partial_y n_e^i})$, where $\overline{\partial_\alpha n_e^i}$ is the α components of the average gradient. Given that there is more than two adjacent cells to the node i an overdetermined system $\mathbf{A}\vec{x} = \vec{b}$ can be formed. In this case a weighted least squares

approach is taken [18]

$$\mathbb{A} = \begin{bmatrix} w_1 & w_1(x_1 - x_i) & w_1(y_1 - y_i) \\ \vdots & \vdots & \vdots \\ w_l & w_l(x_l - x_i) & w_l(y_l - y_i) \\ \vdots & \vdots & \vdots \\ w_N & w_N(x_N - x_i) & w_N(y_N - y_i) \end{bmatrix}, \quad \vec{x} = \begin{bmatrix} n_e^i \\ \frac{\partial n_e^i}{\partial x} \\ \frac{\partial n_e^i}{\partial y} \end{bmatrix}, \quad \vec{b} = \begin{bmatrix} w_1 n_e^1 \\ \vdots \\ w_l n_e^l \\ \vdots \\ w_N n_e^N \end{bmatrix}, \quad (5.2)$$

where

$$w_l = \frac{1}{d_l^P}, \quad d_l = \sqrt{(x_l - x_i)^2 + (y_l - y_i)^2}. \quad (5.3)$$

The parameter P is set to 0.25 following the original article. The system is then solved in the least squares sense using the QR factorization via Householder transformation. The result of QR factorization is an orthonormal matrix \mathbb{Q} and upper triangular matrix \mathbb{R} . Matrix \mathbb{R} is trivially trimmed to size (3×3) and inverted by forward substitution. The solution vector is given by

$$\vec{x} = \mathbb{R}^{-1} \mathbb{Q} \vec{b}. \quad (5.4)$$

Note that at the borders of the domain there are nodes with less than three adjacent cells. In that case the number of cells is artificially augmented taking into account extended neighbourhood of the node as described here [18].

With a gradient computed at the grid nodes the value of the gradient at any given point $(\text{grad } n_e)^{ij}(\vec{x})$ of a face is estimated as a linear interpolation of the gradients at the nodes i, j forming the face

$$(\text{grad } n_e)^{ij}(\vec{x}) = (\text{grad } n_e)^i + |\vec{x} - \vec{x}_i| \frac{(\text{grad } n_e)^j - (\text{grad } n_e)^i}{|(\text{grad } n_e)^j - (\text{grad } n_e)^i|}, \quad (5.5)$$

where $(\text{grad } n_e)^i$ is the gradient value at node i , $(\text{grad } n_e)^j$ is the gradient value at node j and \vec{x}_i is the position of node i .

The gradient computation is here described for the a 2D mesh, but an analogous algorithm could be used in case of 3D simulations.

Chapter 6

Ray tracing algorithm for general meshes

In this chapter, the technical details of the implemented ray tracing algorithm are discussed. The code itself consist of multiple modules, to separate concerns and improve readability and maintainability. Most importantly the algorithm for finding the ray trajectories is separated from the procedures estimating the energy exchanged with plasma. The description is presented in 2D although, most of the algorithm can be used in 3D simulations as is.

6.1 Ray trajectories computation

Initially, the simulated radiation needs to be decomposed to a set of individual rays. A line in space outside of the simulation mesh is chosen. At this line a set of equidistant rays with prescribed direction is generated. Each of these rays is assigned a particular energy by performing a numerical integration of intensity according to (3.5). Beside energy, each of the rays has its own wavelength, although in practice this is usually the same for all rays, when simulating a single laser source.

Each of the rays is then independently traced through the mesh. A single ray is traced using the following steps:

1. An intersection with the boundary of the mesh is found. The boundary is described as a set of faces. For each face given by points A , B , an attempt is made to find an intersection O with a half line defined by the ray origin P and the direction \vec{d} . Denoting \vec{n}_d a normal to \vec{d} and \vec{n}_{AB} a normal to AB , the intersection is found

using the following formula

$$k = \frac{\vec{n}_d \cdot (P - A)}{\vec{n}_d \cdot (B - A)} \quad (6.1)$$

$$t = \frac{\vec{n}_{AB} \cdot (A - P)}{\vec{n}_{AB} \cdot \vec{d}} \quad (6.2)$$

$$O = A + k(B - A), \quad (6.3)$$

where the intersection lies on the face only if parameters k and t fulfill the following inequalities

$$k \geq 0 \wedge k \leq 1 \wedge t \geq 0. \quad (6.4)$$

For illustration, see Fig. 6.1. The direction of the ray on the boundary remains unchanged.

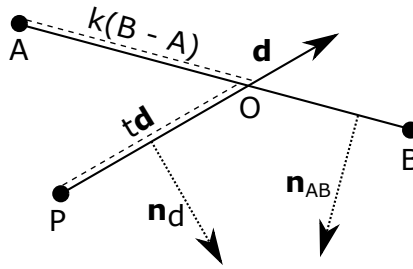


FIGURE 6.1: Intersection O and a face AB with half line \vec{d}

2. A cell adjacent to the face is found and an arbitrary procedure resulting to a point on a face of the cell is performed. In case of cells with assigned constant values of state variables, the index of refraction is assumed to be constant over the whole cell. This results in a ray propagating in a straight line [21] and is resolved by finding an intersection with the cell faces. The same procedure as in step 1. is used. The origin of the half line is the previous intersection and the direction is given by the previous step.
3. In the found point, the electron density gradient is calculated. This is done by employing one of the methods described in chapter 5.
4. Adjacent cells to the newly obtained face are found and a procedure deciding a new direction is called. In case of this work, it is usually a function implementing the Snell's law combined with law of reflection in form of equation (2.4). It is important to note, that the interface between environments with different indices of refraction appearing in the Snell's law, is given by the electron density gradient and not the face itself. This effectively means that in the vector form of Snell's law,

unit vector in the **gradient direction is taken** for \vec{n} . Also, to avoid numerical errors, the ray is only refracted if $(\nabla n_e) \cdot \vec{l} > 0$ meaning that the ray is propagating along the gradient. If a total reflection occurs, the cell previous to this intersection is marked to be later used for resonant absorption.

5. There is no assumption made about the direction returned by the previous procedure. Given the direction, one of two adjacent cells is chosen.
6. Now the simulation returns to step 2. and repeats unless a condition for termination is met. This condition is usually set to the ray leaving the mesh.

Note that in these steps no assumption is made about the type of cells. The same algorithm is used for both triangle and quadrilateral meshes. Also an arbitrary procedure can be used to trace the path inside a cell. This is advantageous as the state variables inside cells might not be constant as is the case in finite difference methods. To enable tracing in higher order finite element domains a new procedure for finding trajectory inside a cell has to be implemented, but the overall algorithm stays the same.

6.2 Comparison with the direct integration

The ray equation (2.1) can be solved using a direct integration method such as the Runge-Kutta fourth order method. To do so, it needs to be rewritten as a set of ordinary differential equations. This is properly done in [21]. It can be shown that using the coordinates (θ, ϕ, n) , where θ is the angle between z -axis and the ray, ϕ is the angle between the ray and x -axis in the xy plane and n is the index of refraction, the unit vector in direction of propagation of the ray is

$$\frac{d\vec{r}}{ds} = (\sin \theta \cos \phi, \sin \theta \sin \phi, \cos \theta). \quad (6.5)$$

The derivation along the ray then has the following form

$$\frac{d}{ds} = \frac{d\theta}{ds} \frac{\partial}{\partial \theta} + \frac{d\phi}{ds} \frac{\partial}{\partial \phi} + \frac{dn}{ds} \frac{\partial}{\partial n}. \quad (6.6)$$

Substituting these into the ray equation (2.1) and performing the necessary algebraic adjustments, a system of ordinary differential equations can be formed [21]

$$\frac{dx}{ds} = \sin \theta \cos \phi \quad (6.7)$$

$$\frac{dy}{ds} = \sin \theta \sin \phi \quad (6.8)$$

$$\frac{dz}{ds} = \cos \theta \quad (6.9)$$

$$\frac{d\theta}{ds} = \frac{\cos \theta}{n} \left(\cos \phi \frac{\partial n}{\partial x} + \sin \phi \frac{\partial n}{\partial y} \right) - \frac{\sin \theta}{n} \frac{\partial n}{\partial z} \quad (6.10)$$

$$\frac{d\phi}{ds} = \frac{1}{n \sin \theta} \left(\cos \phi \frac{\partial n}{\partial y} - \sin \phi \frac{\partial n}{\partial x} \right). \quad (6.11)$$

To simplify the system, a solution in the plane yz is considered. By setting $\phi = \pi$ the system reduces to

$$\frac{dy}{ds} = \sin \theta \quad (6.12)$$

$$\frac{dz}{ds} = \cos \theta \quad (6.13)$$

$$\frac{d\theta}{ds} = \frac{1}{n} \left(\cos \theta \frac{\partial n}{\partial y} - \sin \theta \frac{\partial n}{\partial z} \right). \quad (6.14)$$

In a special case of linear dependence of index of refraction $n = Cz$, the system has the form $\frac{d\vec{\xi}}{ds} = \vec{f}(\vec{\xi})$

$$\frac{d}{ds} \begin{bmatrix} y \\ z \\ \theta \end{bmatrix} = \begin{bmatrix} \sin \theta \\ \cos \theta \\ -\frac{\sin \theta}{z} \end{bmatrix} \quad (6.15)$$

and can be solved using the Runge-Kutta fourth order method.

To compare the solution obtained by this direct integration with the ray tracing algorithm a special form of electron density profile needs to be chosen and collisions must be neglected by setting ionization to 0. Setting electron density profile to

$$n_e = n_e^{crit}(1 - z^2) \quad (6.16)$$

and neglecting collisions results to permittivity (2.5) equal to

$$\varepsilon = 1 - \frac{\omega_p^2}{\omega^2} = 1 - \frac{n_e}{n_e^{crit}} = z^2 \quad (6.17)$$

and thus the index of refraction

$$n = \sqrt{\varepsilon} = |z|. \quad (6.18)$$

Using this profile, the ray turning z_t point can be analytically determined. It is

$$z_t = 1 - \sin \theta_0, \quad (6.19)$$

where θ_0 is the initial angle of incidence of the ray. The electron density of the plasma at this point is referred to as the effective critical density and is equal to

$$n_e(z_t) = n_e^{crit}(2 \sin \theta_0 - \sin^2 \theta_0). \quad (6.20)$$

The comparison of the solutions using the density profile (6.16) for various initial conditions (y_0, z_0, θ_0) (θ_0 being the parameter of interest) on a random triangular mesh has been done. This is summarized in Fig. 6.2 for θ_0 equal to 0.1 and 0.2 rad and in Fig. 6.3 for θ_0 equal to 0.25 and 0.5 rad. The choice of angles of incidence is the same as in [21] to enable direct comparison.

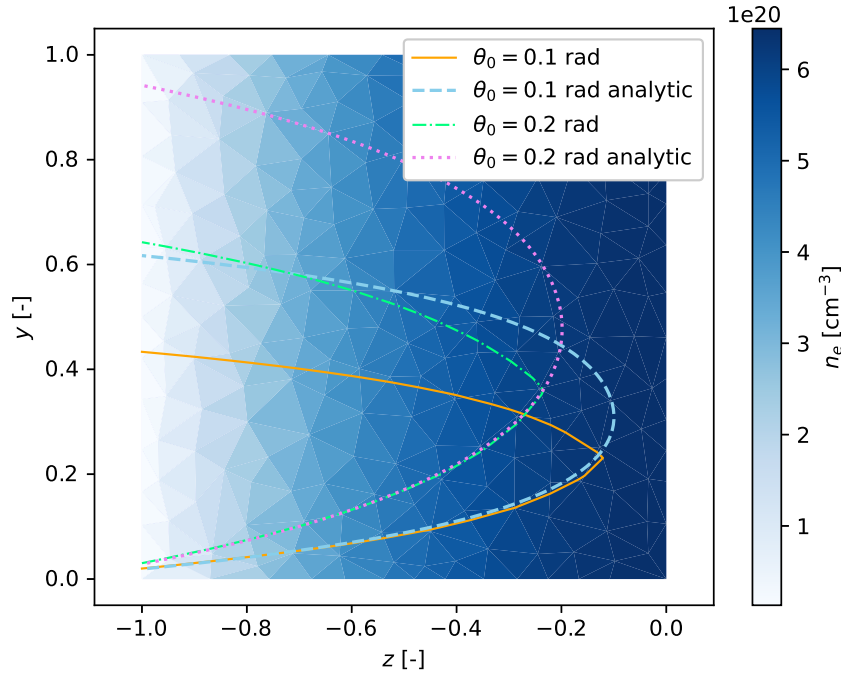


FIGURE 6.2: Ray tracing compared with direct integration for initial angel of incidence θ_0 equal to 0.1 and 0.2 rad

It can be seen that the ray tracing follows the directly integrated solution until a near effective critical density given by (6.20) at position (6.19) is reached. Here, the conditions for total reflection given by negative radicand in equation (2.4) are met and the ray makes a sharp turn. This is a known effect of this type of method. The results are similar to those in [21].

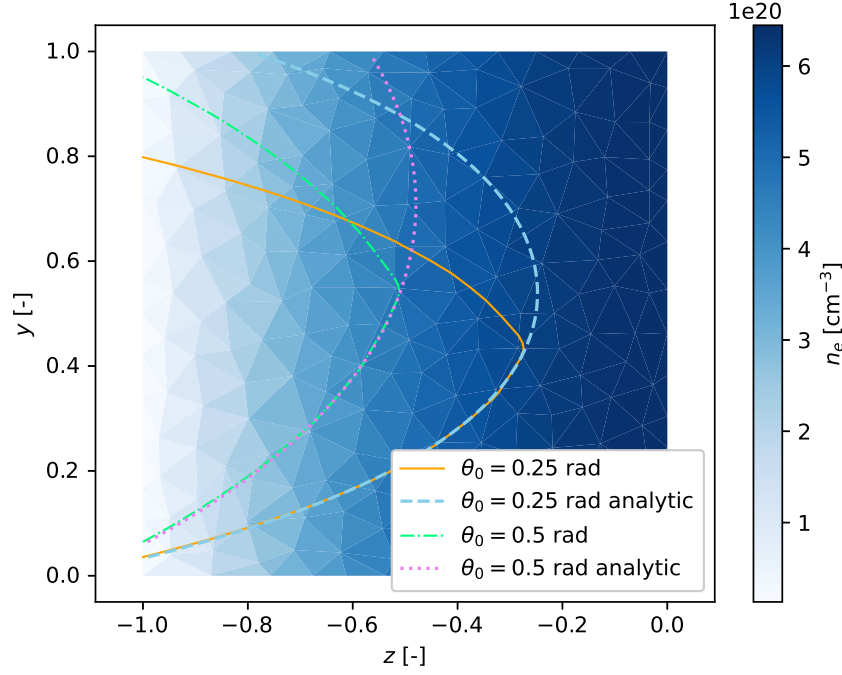


FIGURE 6.3: Ray tracing compared with direct integration for initial angle of incidence θ_0 equal to 0.25 and 0.5 rad

For simulations of laser absorption, the key parameter is the depth of penetration. This equals to direct integration result with precision equal to the mean cell size. The cell size plays a major role as the condition is met on the first encountered face of cell with density higher than effective critical density.

6.3 Ray energy exchange estimation

After the ray trajectories are found, the energy changes along these trajectories are estimated. For a single ray this is achieved by iterating over intersections and calculating the amount of exchanged energy in each intersected cell.

To approximate the amount of energy absorbed via inverse bremsstrahlung the following formula is used in each cell the ray intersects

$$\Delta E = E_{in} (1 - \exp(-k_{ib}|O_1 - O_2|)) \quad (6.21)$$

where O_1 and O_2 are the intersections with the cell $|O_1 - O_2|$ is the length of the ray in the cell, and E_{in} is the energy of the ray entering the cell. This stems directly from equation (3.3) using the bremsstrahlung coefficient k_{ib} defined by (3.7) evaluated using

temperature and ionization in the cell. The value ΔE is then subtracted from the ray energy and the algorithm continues to another cell.

Energy absorbed through resonant absorption is localized to a single cell. This cell was marked in step 4. of the ray tracing algorithm. The amount of energy absorbed is given by equation (3.15).

Chapter 7

Simulations of radiation propagation

In the previous work [22], a 1D hydrodynamic simulation of laser interaction with solid target was performed. The new M-level model is used to predict x-ray gain coefficient. The results are then extended to 2D by assuming a symmetry in direction parallel to the plane of the solid target. It turns out that x-ray laser propagation in this plasma is not significantly affected by diffraction effects, a fact that is be further discussed. To demonstrate the application of the developed algorithm to 2D x-ray intensity estimation based on x-ray amplification model described in [chapter 3](#), tracing of straight rays parallel to the target surface is performed.

7.1 Results of 1D hydrodynamic simulation

A simulation first described in [19] has been performed in previous work [22]. The simulation deals with three incoming driving laser pulses interacting with a solid iron target. The wavelength of the driver is 800 nm. The three laser pulses are specified in time using the time of peak intensity τ , full width at half maxima FWHM and peak intensity I . These parameters are summarized in Tab. 7.1.

First pulse	Second pulse	Third pulse
$\tau = 1.5$ ns	$\tau = 2.0$ ns	$\tau = 2.51$ ns
$\Delta_{FWHM} = 1.0$ ns	$\Delta_{FWHM} = 0.1$ ns	$\Delta_{FWHM} = 0.5$ ps
$I = 1.25 \cdot 10^{11}$ W·cm ⁻²	$I = 1.25 \cdot 10^{12}$ W·cm ⁻²	$I = 1.16 \cdot 10^{15}$ W·cm ⁻²

TABLE 7.1: Parameters of the hydrodynamic simulation, τ is the time of arrival, Δ_{FWHM} is full width at half maxima and maximal intensity I

The initial conditions are set to match the conditions in solid iron at room temperature. Ion and electron temperatures are set to 0.03 eV, initial mass density is $7.87 \text{ g} \cdot \text{cm}^{-3}$. The initial thickness of the target is only 52 nm to avoid simulating non ablating cells. As for boundary conditions, the left boundary is a wall governed by zero velocity and the right boundary condition is specified by pressure of 0.1 Pa allowing the plasma to expand. Artificial viscosity and heat flux limiter are used during the simulation. A quotidian equation of state (QEOS) [14] is used. This is crucial as the ionization plays a major role when determining the gain coefficient. The start of the simulation is marked by time 0 and the end of the simulation is set to 2.54 ns. The results of the 1D simulation are shown in Fig. 7.1. The full description of the results is in the previous work [22].

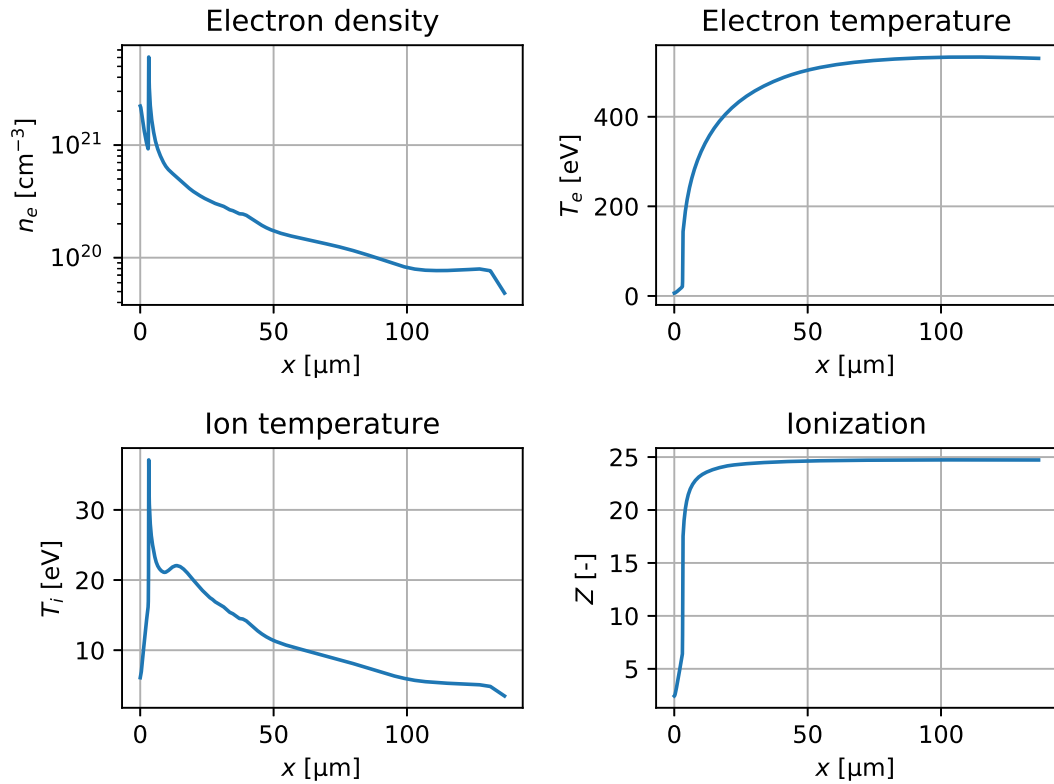


FIGURE 7.1: Result of 1D hydrodynamic simulation at time 2.54 ns of three incoming laser pulses with wavelength 800 nm

7.2 Gain prediction in 1D hydrodynamic simulation

Previously, the hydrodynamic simulation was post processed using a simplistic three level system to estimate the gain coefficient at a specific wavelength of x-ray radiation. The transition of concern is (3.18) and has the wavelength of 25.5 nm. In this work, a more sophisticated M-level model described in chapter 3 is used. Specifically, 240 energy

levels in neon-like iron are taken into account with principal quantum number up to 6. It is applied on the result of the 1D hydrodynamic simulation summarized briefly in the previous section.

In Fig. 7.2, a comparison is made with the results obtained in the previous work. Both the absolute gain profiles and relative gain profiles are contrasted. As is already pointed out in chapter 3, the predicted absolute gain values are approximately five time smaller then using the 3-level system, but the profiles are fairly similar. This is partially explained by the fact, that the profile is largely influenced by the fractional abundance of neon like ions, which is modeled in the same way in both cases.

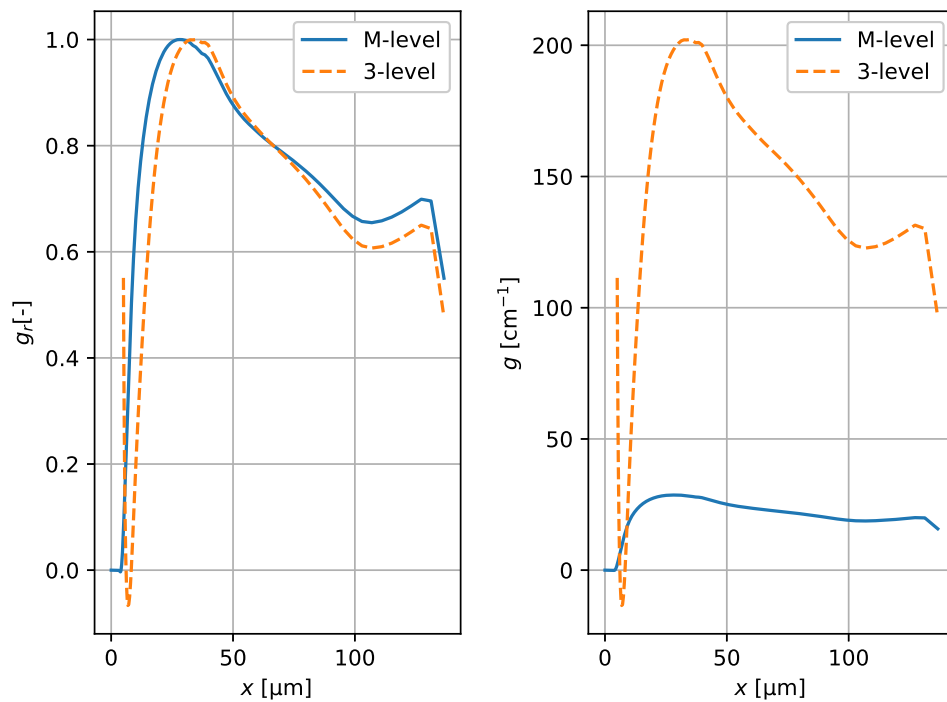


FIGURE 7.2: Comparison of gain profiles emerging from post processing of the 1D hydrodynamic simulation using the 3-level system and M-level system. In the left image is a comparison of relative gain profiles g_r and in the right image are the actual gain values g

The actual difference in the model is mainly in the computation of the relative population inversion. To highlight this, the relative population inversion is compared in Fig. 7.3. This is also done using the normalized inversion and the actual relative inversion (here relative is in the context of abundance of the neon like ions). The normalized profiles are comparable, except for the area close to the target on the left. There are no conditions for the levels of interest to be populated at all. While the more sophisticated M-level simulation can deal with this fact very well as many other levels are taken into account, the simplistic 3-level method fails to produce physically relevant results.

To summarize, the M-level model points to some flaws in the 3-level approximation. Most importantly, to the assumption that most of the population is located at these three levels. This leads to overestimation of the relative inversion by a factor of five in our particular case. The fact that otherwise the profiles are remarkably similar is very valuable as for the applicability of the 3-level model where a simple and fast solution is required. However, caution must be taken when it comes to absolute values of level populations.

The main benefit of the M-level system is its ability to provide relevant predictions in plasma regions with zero or negative gain coefficient. This may prove valuable in full multidimensional hydrodynamic simulations.

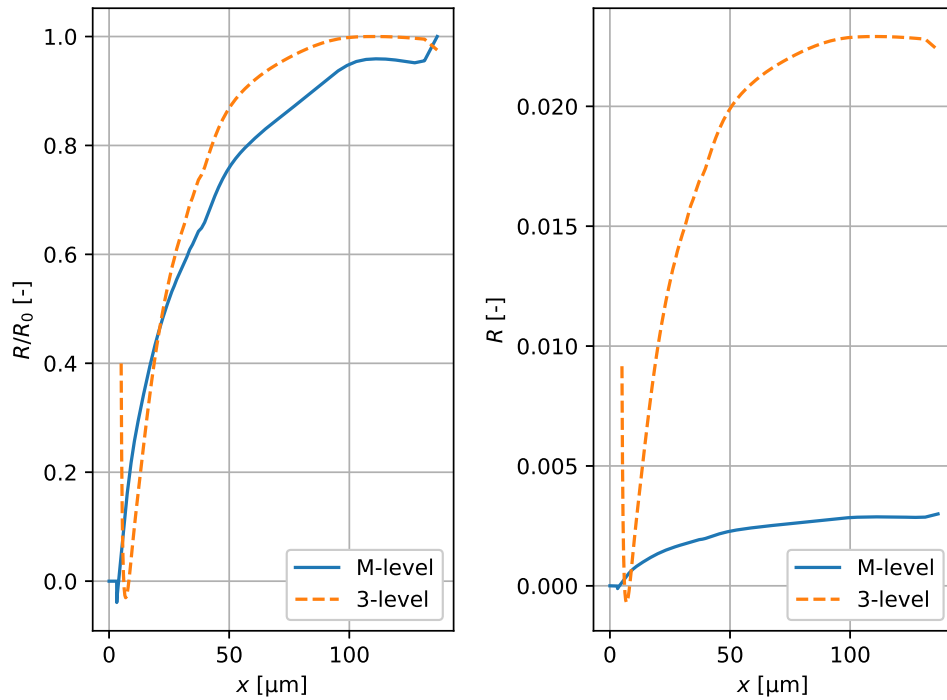


FIGURE 7.3: Relative populations inversion R used for gain predictions. On the left is a normalized profile and on the right is the actual relative inversion

7.3 Extension of the 1D results to 2D

To enable 2D ray tracing simulations, the results of 1D hydrodynamic simulation is extended to 2D by assuming a symmetry in direction parallel to the target. This is achieved by creating a quadrilateral mesh with 200 cells of size given by 1D Lagrangian simulation in x direction and 200 equidistant nodes in y direction. Values of state functions are mapped accordingly to 1D simulation. To illustrate this, part of the mesh

and mapped gain coefficient, obtained using the M-level model, are shown in Fig. 7.4. The whole mesh is 1 mm wide and almost 140 μm long (width is in the y direction). The width of the mesh is chosen based on the results of simulations [19].

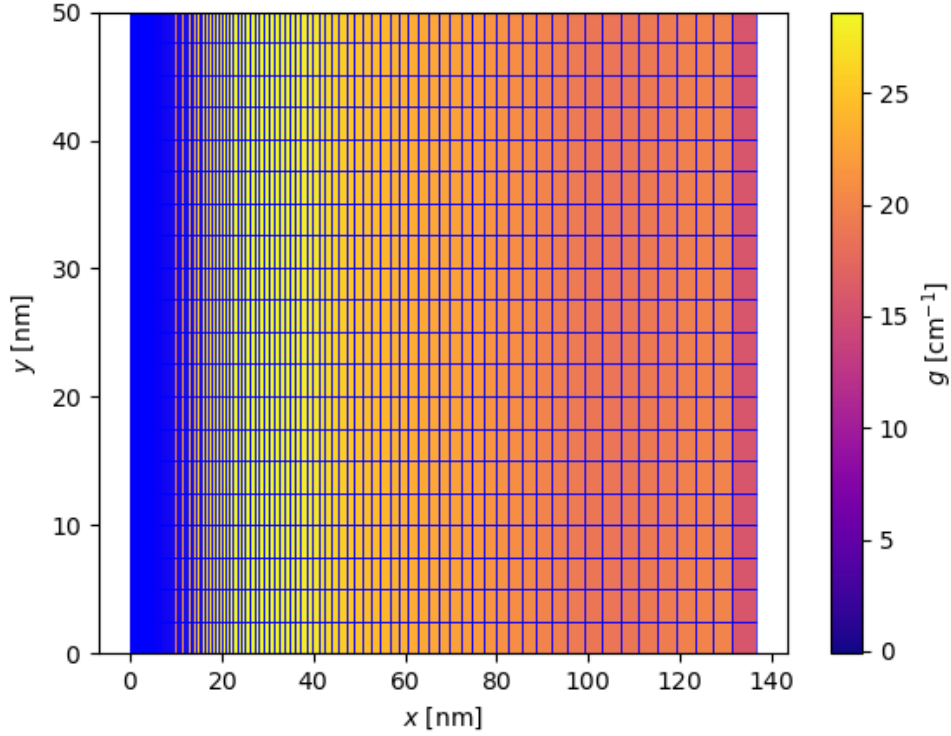


FIGURE 7.4: Gain coefficient g mapped on a 2D mesh created by extension of 1D results

7.4 Driving laser absorption simulation

Using the mapped results, a 2D ray tracing of a driving laser with wavelength 800 nm has been performed. This demonstrates the capability of the implemented algorithm to predict absorbed energy of the driving laser in a 2D hydrodynamic simulations.

First, a driving laser with angle of incidence 30° is examined. The trajectories have been found for 10000 rays, beginning at a line segment defined by points $(140, -50) \mu\text{m}$ and $(140, -10) \mu\text{m}$. The spatial intensity $I_{\Delta t}$ is assumed to be Gaussian normalized to 1 with $\Delta_{FWHM} = 10 \mu\text{m}$. This means that after distributing the energy among the rays, using equation (3.5), the combined energy of all rays is equal to 1 (in arbitrary energy units). The initial direction of all the rays is set to a given vector.

The trajectories have been post processed using the models of inverse bremsstrahlung and resonant absorption described in chapter 3. Both the trajectories and the resulting

absorbed energy are demonstrated in Fig. 7.5. For obvious reasons, not all trajectories are displayed, only a representative sample. Zoomed images of trajectories with temperature and electron density profiles are also added.

The amount of absorbed energy is 83.1%. It turns out that the energy is absorbed exclusively via bremsstrahlung as the amount of energy absorbed via resonant absorption is 15 orders of magnitude smaller. This confirms the results in [21], although no proper comparison is possible as the hydrodynamic simulation being processed is different and in this work no time evolution of the system is examined.

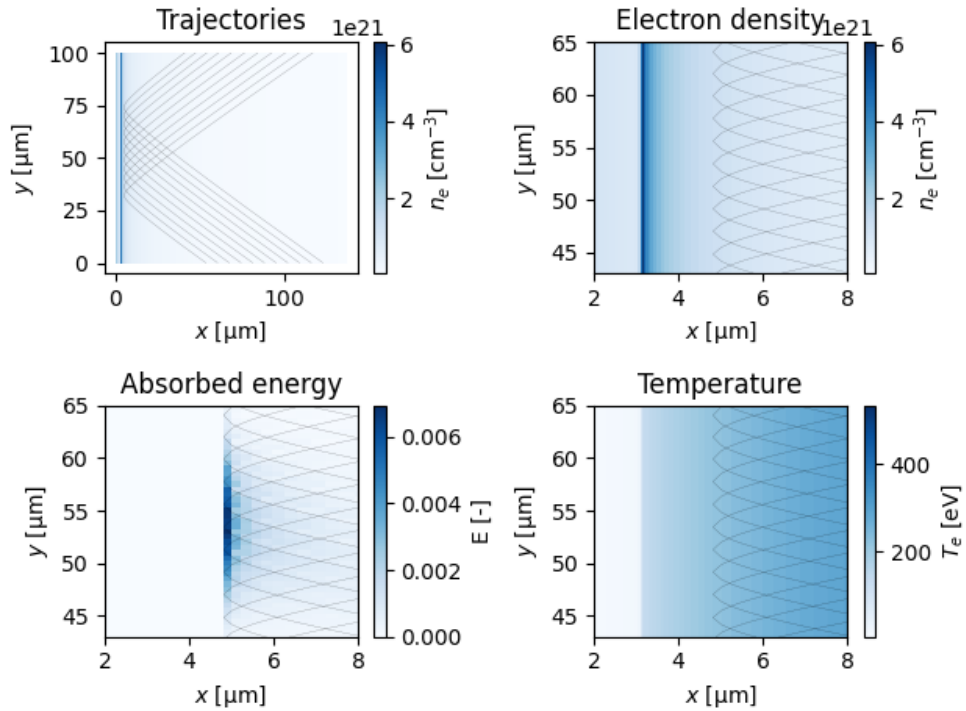


FIGURE 7.5: Driving laser with angle of incidence 30° . In the top left and top right images are the trajectories with the electron density n_e as background. In the bottom left image the absorbed energy is displayed and in the bottom right image the electron temperature T_e is used as background for the trajectories

To investigate the relevance of resonant absorption, a set of lasers with various angles of incidence has been simulated. To demonstrate the capability of the implemented algorithm to simulate multiple lasers at once, this has been done in a single simulation. The trajectories have been once more post processed with resonant absorption and bremsstrahlung models. The best results were obtained for small angles, namely angles of incidence $\theta_1 = 1^\circ$, $\theta_2 = 2^\circ$, $\theta_3 = 3^\circ$ and $\theta_4 = 5^\circ$. This is shown in Fig. 7.6, where the absorbed energy and a sample of trajectories of each laser is presented.

The absorbed energies and the amount absorbed via each mechanism are shown in Tab. 7.2. Most of the energy, 96.5 %, has been absorbed for angle of incidence 3° , in

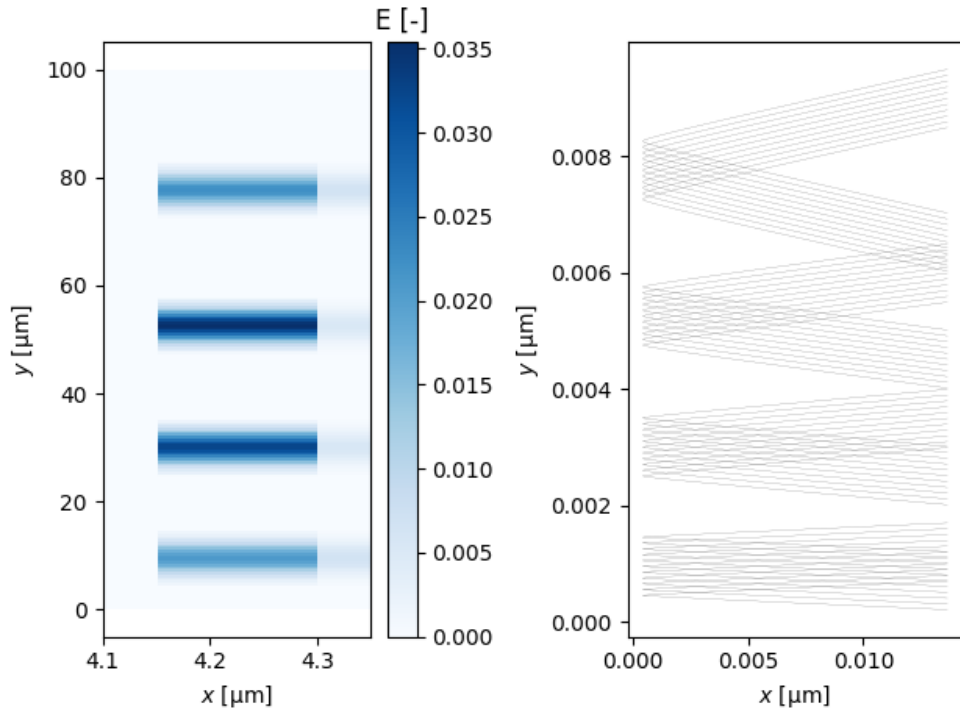


FIGURE 7.6: Absorption of rays with angles of incidence, from bottom to top: $\theta_1 = 1^\circ$, $\theta_2 = 2^\circ$, $\theta_3 = 3^\circ$ and $\theta_4 = 5^\circ$. In the left panel is shown the zoom of the area of resonant absorption and in the right panel the whole trajectories are shown.

this case 27.3% of initial energy has been absorbed via resonance. It is expected that resonant absorption is relevant for small angles of incidence [21], but it is also important to point out that for even smaller angles, the resonant absorption decreases rapidly as the parameter q in equation (3.15) approaches zero.

θ [°]	1	2	3	5
e_b [%]	79.5	71.3	69.2	79.5
e_r [%]	9.8	23.6	27.3	10.9
total e [%]	89.3	94.9	96.5	90.4

TABLE 7.2: Fraction of energy absorbed via bremsstrahlung e_b , resonance e_r and the total energy absorbed e for angles of incidence θ

7.5 X-ray gain simulations in laser generated plasma

In the previous section, the ray tracing algorithm has been used to find the trajectories of rays obtained by decomposing the driving laser in a plasma generation simulation. The capability of the same algorithm to simulate x-ray amplification is demonstrated. This is performed over the results of 1D simulation extended to 2D the same way as in previous sections. The only difference is the width of the target, which is 1 mm in

this case. The cell counts remain unchanged. An X-ray laser of wavelength 25.5 nm propagation is simulated in direction parallel or almost parallel to the surface of the target.

First, a laser beginning at a line segment given by points (10, -1) μm and (140, -1) μm in direction exactly parallel to the target surface is simulated. The initial line segment is chosen to cover the area of the maximal gain coefficient. The simulation is performed for 10000 rays. This is done to check the implementation and to obtain a reference result. In this case, no refraction effect can even happen, because the rays never encounter a cell with different state variables as the previous. The straight trajectories are depicted in Fig. 7.7.

In this case the amount of energy gained by the laser E_g can be in theory analytically evaluated using the equation (3.17) and the width of the target for each of the rays, but this is exactly what the post processing algorithm does in case of straight trajectories parallel to the target surface. An interesting value is the total amount of energy gained. In this case the initial energy of the laser is 1 and the energy gained is 16.1 in arbitrary units. Over the width of 1 mm, this is equal to mean gain coefficient of 28.4 cm^{-3} which agrees with the used gain profile.

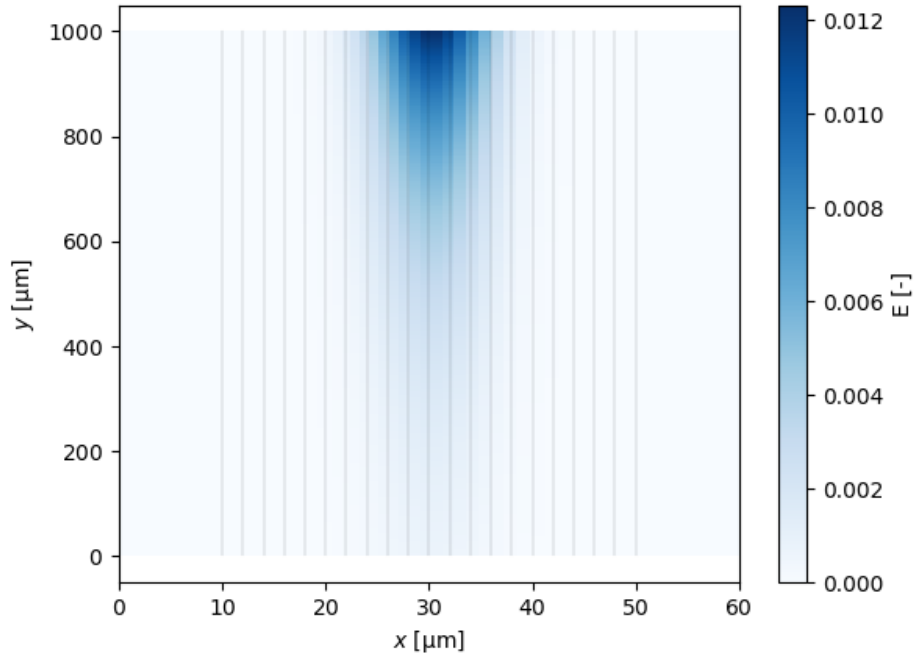


FIGURE 7.7: Energy gained and trajectories of the the x-ray laser propagating parallel to the target

Next, a very similar simulation is performed, now assuming a small shift in the initial direction. The x-ray laser is skewed towards the target by 5 mrad. The angle value is

taken based on the experiments [4], where a refraction shift of this order is expected. The resulting trajectories and gained energy are shown in Fig. 7.8.

Although by looking at the graph, the results seem to vary slightly, the total energy gained is the same as in the case of the rays propagating exactly parallel to the surface of the target. It is important to keep in mind that very different scales are used on the axes parallel and perpendicular to the target surface, when interpreting the figure. The apparent refraction of the rays in the area of higher electron density is very small. In this simplistic case, no significant role of diffraction on energy gain values has been identified, but the ability to simulate refraction effects has been demonstrated. As stated in [19], for diffraction to play a significant role, the width of the target would have to be in order of mm. This explains the negligible effect of refraction and the results are in good agreement with [19].

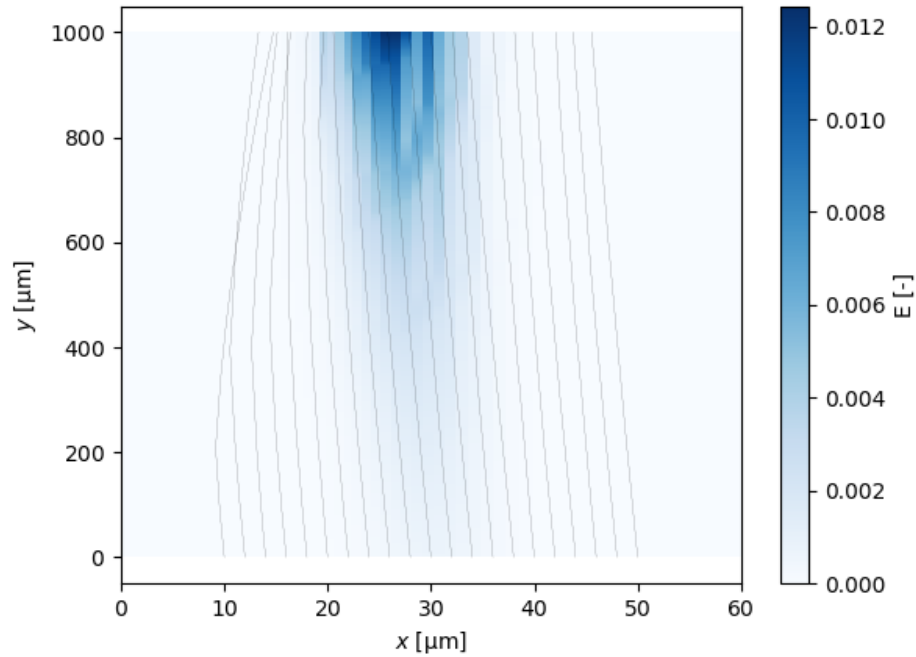


FIGURE 7.8: Energy gained and trajectories of the x-ray laser propagating under a small angle towards the target

Chapter 8

Conclusion

An effort to generalize the previous simulations of soft X-ray laser amplified in conventional laser generated plasma was described in this work.

A theoretical framework was established and basic assumptions were stated. A general approach to plasma and radiation interaction was taken to enable both the driving laser and seeding pulse simulations. Previously developed 3-level model used to describe X-ray amplification in laser generated plasma was generalized to M -level system. Differences between the previous and current approach were pointed out and the influence on resulting gain coefficient profile was assessed.

The domain discretization techniques were summarized and a method for gradient estimation was described to enable the tracing of laser rays in discrete domains of relevant hydrodynamic simulations.

Finally, a ray tracing algorithm for general meshes with energy exchange estimation was implemented. With this algorithm the results of 1D simulation extended to 2D by assuming a symmetry was post processed. Both, the capability to model radiation energy absorption and radiation energy amplification were demonstrated. The results of the simulations were compared with similar works and analytical predictions.

Bibliography

- [1] W. S. Abdelaziz. Calculation of Atomic Data and Gain Coefficient for XUV & Soft X-Ray Laser Emission from Ge XXIII. *Optics and Photonics Journal*, 04(09):246–269, 2014.
- [2] Max Born and Emil Wolf. *Principles of optics: electromagnetic theory of propagation, interference and diffraction of light*. Pergamon Press, Oxford ; New York, 6th ed edition, 1980.
- [3] E. J. Caramana, D. E. Burton, M. J. Shashkov, and P. P. Whalen. The Construction of Compatible Hydrodynamics Algorithms Utilizing Conservation of Total Energy. *Journal of Computational Physics*, 146(1):227–262, October 1998.
- [4] T. Ditmire, M. H. R. Hutchinson, M. H. Key, C. L. S. Lewis, A. MacPhee, I. Mercer, D. Neely, M. D. Perry, R. A. Smith, J. S. Wark, and M. Zepf. Amplification of xuv harmonic radiation in a gallium amplifier. *Physical Review A*, 51(6):R4337–R4340, June 1995.
- [5] Veselin A. Dobrev, Tzanio V. Kolev, and Robert N. Rieben. High-Order Curvilinear Finite Element Methods for Lagrangian Hydrodynamics. *SIAM Journal on Scientific Computing*, 34(5):B606–B641, January 2012.
- [6] K. Eidmann, J. Meyer-ter Vehn, T. Schlegel, and S. Hüller. Hydrodynamic simulation of subpicosecond laser interaction with solid-density matter. *Physical Review E*, 62(1):1202–1214, July 2000.
- [7] Shalom Eliezer. *The interaction of high-power lasers with plasmas*. Series in plasma physics. Institute of Physics Publishing, Bristol, 2002.
- [8] Andrew S. Glassner and Association for Computing Machinery, editors. *An introduction to ray tracing*. Kaufmann, San Francisco, Calif, digital print edition, 2007.
- [9] M. F. Gu. The flexible atomic code. *Canadian Journal of Physics*, 86(5):675–689, May 2008.
- [10] P. B. Holden, S. B. Healy, M. T. M. Lightbody, G. J. Pert, J. A. Plowes, A. E. Kingston, E. Robertson, C. L. S. Lewis, and D. Neely. A computational investigation of the neon-like germanium collisionally pumped laser. *Journal of Physics B: Atomic, Molecular and Optical Physics*, 27(2):341–367, January 1994.

- [11] Pierre Jaegle. *Coherent Sources of XUV Radiation*, volume 106 of *Optical Sciences*. Springer New York, New York, NY, 2006.
- [12] M. Kuchařík. *Arbitrary Lagrangian-Eulerian (ALE) Methods in Plasma Physics*. Doctoral Thesis, Czech Technical University, Prague, 2006.
- [13] R. Liska, M. Kuchařík, J. Limpouch, O. Renner, P. Váchal, L. Bednárik, and J. Velechovský. ALE Method for Simulations of Laser-Produced Plasmas. In Jaroslav Fořt, Jiří Fürst, Jan Halama, Raphaële Herbin, and Florence Hubert, editors, *Finite Volumes for Complex Applications VI Problems & Perspectives*, Springer Proceedings in Mathematics, pages 857–873, Berlin, Heidelberg, 2011. Springer.
- [14] R. M. More, K. H. Warren, D. A. Young, and G. B. Zimmerman. A new quotidian equation of state (QEOS) for hot dense matter. *The Physics of Fluids*, 31(10):3059–3078, October 1988.
- [15] J. Nikl. Some aspects of numerical methods for laser plasma hydrodynamics. Master’s thesis, Czech Technical University, 2017.
- [16] J. Nikl. *Modelling of non-local energy transport in plasma*. Dissertation study, Czech Technical University, Prague, 2020.
- [17] J. Nikl, M. Kucharik, M. Holec, and S. Weber. Curvilinear high-order Lagrangian hydrodynamic code for the laser – target interaction, 2018.
- [18] H. Nishikawa and J. A. White. An efficient cell-centered finite-volume method with face-averaged nodal-gradients for triangular grids. *Journal of Computational Physics*, 411:109423, June 2020.
- [19] E. Oliva, P. Zeitoun, P. Velarde, M. Fajardo, K. Cassou, D. Ros, S. Sebban, D. Portillo, and S. le Pape. Hydrodynamic study of plasma amplifiers for soft-x-ray lasers: A transition in hydrodynamic behavior for plasma columns with widths ranging from $20\mu\text{m}$ to 2 mm. *Physical Review E*, 82(5):056408, November 2010.
- [20] G. J. Pert. The analytic theory of linear resonant absorption. *Plasma Physics*, 20(3):175–188, March 1978.
- [21] J. Velechovský. *Modelling of laser radiation absorption in plasma*. Research report, Czech Technical University, 2010.
- [22] M. Šach. *Hydrodynamic Plasma Simulations for X-Ray Laser Realization*. Bachelor thesis, Czech Technical University, 2019.